JOURNAL OF AIRCRAFT
Vol. 42, No. 4, July–August 2005

Numerical Investigation of Nonlinear Aeroelastic Effects on Flexible High-Aspect-Ratio Wings

Joseph A. Garcia*
NASA Ames Research Center, Moffett Field, California 94035-1000

A nonlinear aeroelastic analysis is developed to analyze the aeroelastic characteristics of flexible high-aspect-ratio wings at transonic speeds. This is achieved by directly coupling a three-dimensional geometric nonlinear methodology, based on a 12 degree-of-freedom beam finite element, with an Euler/Navier–Stokes computational fluid dynamics analysis. Static aeroelastic results are presented for an unswept and swept high-aspect-ratio wing. Unswept wing results show a reversal in twist due to the nonlinear torsion–bending coupling effects. Specifically, the torsional moments due to drag become large enough to cause the wing twist rotations to washin the wing tips, whereas the linear results show a washout twist rotation. The nonlinear twist results are attributed to the large bending displacements coupled with the large drag experienced by this flexible high-aspect-ratio wing at the transonic flow conditions. Swept wing results show that nonlinear torsion–bending effects tend to reduce the amount of washout as compared to a linear structural aeroelastic analysis, making the wing more prone to tip stall.

Nomenclature

C_l, C_d, C_s = lift, drag, and side force coefficients
C_m = pitching moment coefficient
EA = axial stiffness
EI_y = lateral bending stiffness
EI_z = transverse bending stiffness
F_{drag}, F_{side}, F_{lift} = computational fluid dynamics forces in the $\bar{x}$, $\bar{y}$, and $\bar{z}$ axes
F_x, F_y, F_z = finite element method forces in the x, y, and z axes
GJ = torsional stiffness
$[G]$ = global structural damping matrix in reference coordinates
J = Jacobian matrix
$[K_G]$ = global stiffness matrix in reference coordinates
L = length of the beam finite element
M = Mach number
M_x, M_y, M_z = torsion, transverse, and lateral moments about x, y, and z axes
$[M]$ = global structural mass matrix in reference coordinates
q = dynamic pressure
$\boldsymbol{q}_i$ = generalized displacement vector
Re = Reynolds number
S = axial force
U = strain energy
u, v, w = axial, transverse, and lateral displacements in x, y, and z directions
W = virtual work
x, y, z = structural reference coordinates
$\bar{x}$, $\bar{y}$, $\bar{z}$ = aerodynamic reference coordinates
y^+ = wall distance in boundary-layer coordinate
$\{Z\}$ = consistent nodal aerodynamic loading vector
γ = specific heat ratio
$\{\delta_e\}$ = local nodal displacement vector
η = nondimensional semispan coordinate
Θ_2 = second-order twist due to beam kinematics
θ = transverse rotation about the z axis
Λ = lateral rotation about the y axis
ν_w = viscosity at the wall
ρ = density
τ_w = shear stress at the wall
ϕ = twist rotation about the x axis

Introduction

FLEXIBLE high-aspect-ratio wings have the potential to undergo large deflections, which under certain flight conditions can reach the geometric nonlinear range of the wing structure. This nonlinearity is especially attainable on uninhabited high-altitude long-endurance (HALE) aircraft. At high altitude, low air densities dictate the use of large wing area and light structural design to increase lift and endurance leading to the design of flexible high-aspect-ratio wings.

In the past decade, the study of uninhabited high-altitude aircraft for use in military reconnaissance and remote sensing has gained importance.[1,2] The U.S. Air Force Research Laboratory has stated that the aerodynamic efficiency of the wing design can be improved by more than 10% by optimizing the lift-to-drag (L/D) ratio, which in turn could increase the mission duration (endurance) of the aircraft by as much as 10% (Ref. 2). Thus, it is crucial to model the nonlinear aeroelastic effects accurately and allow the aircraft designer to optimize the wing structure without compromising aerodynamic performance.

Current studies on aircraft with high-aspect-ratio wings have focused on subsonic flow conditions.[3–7] In these subsonic studies, it has been shown that there are significant differences between the dynamic aeroelastic characteristics of flexible high-aspect-ratio wings using a linear structural analysis vs a nonlinear structural analysis.[6] However, HALE technology developments show a trend toward operating at higher altitudes and faster speeds. As an aircraft reaches higher altitudes, the speed of sound decreases. This decrease in sound speed will produce higher Mach numbers without an increase in speed. Once the flow Mach numbers on the wing reach the transonic regime, aircraft designers will need to predict properly the nonlinear effects of the flow, such as shock–boundary-layer interaction, to predict accurately and understand the aerodynamic performance of the aircraft. Furthermore, Reynolds number decreases with increasing altitude, making the boundary layer on the wing more susceptible to separation.[8] The coupling of a nonlinear structural model to a high-fidelity nonlinear fluid dynamics model is needed to analyze the nonlinear aeroelastics accurately at transonic speeds. This need has recently been identified by the Airframe Technology Advisory Group, which was formed under the

---

Received 19 November 2003; revision received 5 March 2004; accepted for publication 10 March 2004.

*Aerospace Engineer, Mail Stop 258-1, Systems Analysis Branch. Member AIAA.

national Fixed Wing Vehicle Program, to identify elements of "precompetitive airframe technology."[9] One specific real-world nonlinear dynamic aeroelastic problem investigated by this group involved aileron buzz on the Global Hawk.[9] The Global Hawk is a HALE unmanned aerial reconnaissance system used by the U.S. military. In this Global Hawk investigation, several computational fluid dynamics (CFD) codes were used to predict the nonlinear aerodynamics and a linear NASTRAN model was used to approximate the structural aileron buzz condition. One of the conclusions of this group was the need for nonlinear structural capability coupled to high-fidelity nonlinear CFD.

As HALE aircraft community ventures into the transonic/supersonic speed regime, they will also need to consider sweptback wing designs. Sweptback wings allow the use of subsonic or transonic airfoil sections at Mach numbers higher than they were designed to operate in.[10] Sweptback wings have the additional linear aeroelastic effects of twist due to bending,[11] as well as changing the wing's static aeroelastic characteristics, such as divergence, control surface reversal, and onset of buffet pitch-up.[11] These swept wing aeroelastic concerns will be complicated by nonlinear aeroelastic torsion–bending coupling when large deflections are involved. Furthermore, at transonic speeds, the flow over the wing can experience significant viscous effects, such as boundary-layer separation and wing buffet. Understanding these viscous effects is particularly important when the wing is operated at off-design conditions with resulting off-design aeroelastic deformations.

This paper begins with a presentation of the governing equations for the new nonlinear aeroelastic analysis and the numerical schemes used. Next, a discussion of the computational mesh for both the structures and the aerodynamics is presented. The aeroelastic coupling approach and grid movement schemes are then discussed. Validation results of the nonlinear aeroelastic analysis are presented for a transonic aeroelastic wing geometry and compared with existing experimental data. In addition, the nonlinear aeroelastic responses of a flexible high-aspect-ratio wing at transonic speeds with and without sweep are investigated.

Governing Equations

The nonlinear aeroelastic analysis is based on the coupling of a three-dimensional geometric nonlinear finite element method (FEM) to an existing nonlinear CFD flow solver[12] using a direct approach. The three-dimensional finite element approach, based on a 12-degree-of-freedom (DOF) beam element, is capable of modeling the structural geometric nonlinear bending displacements, as well as the nonlinear torsion–bending coupling for high-aspect-ratio wings. See Ref. 13 for further details.

The aerodynamic equations of motion used in the CFD flow solver are based on the Reynolds-averaged Navier–Stokes equations. Because of the presence of crossflow and transonic shocks, a strong conservation law form of the Navier–Stokes equations is used. To resolve the high-gradient flow features normal to the body surface, present in high Reynolds number viscous flows, the spatial grid resolution is highest in the body-normal direction. This leads to the use of the thin-layer Navier–Stokes equations, which retain the viscous terms normal to the body and neglect the viscous terms along the body. Details of the governing aerodynamic equations can be found in Ref. 13.

The structural equations of motion are based on classical beam theory. The assumptions that form the bases of classical beam theory are as follows. 1) The beam is much longer in one direction. 2) The cross sections remain planar; therefore, the beam sections remain normal to the beam elastic axis. 3) The slope of the beam is small, and the square of the slope is neglected in the curvature equations. However, as the beam is bent to large displacements, the theory is no longer accurate, and solving the exact curvature formulation of the beam becomes necessary. Solving the exact analytic curvature formula for a beam can become especially complicated for a three-dimensional beam with nonuniform properties. In previous works by Hodges and Dowell,[14] as well as by Minguet and Dugundji,[15] the exact beam equations were solved. However, the approach taken in this study is to use the FEM[16] to analyze the governing equations of motion for the beam. In the finite element approach, the structure is subdivided into a number of elements and the variational approach for calculating the stiffness matrix is used, based on the principle of virtual displacements,[17] to approximate the elastic response of the structure over each element. The advantage of using the FEM approach is its ability to model nonuniform structural properties, arbitrary geometry, complex loading, and boundary conditions. The type of element chosen to model the flexible high-aspect-ratio wing is a three-dimensional beam element, also known as a space frame element.[18] The structural stiffness is obtained by forming the conventional linear stiffness for small deflections along with a geometric stiffness to account for the effects of large displacements. The nonlinear geometric displacement path is then obtained by using an incremental load approach and performing three-dimensional Euler transformations at each incremental step. This approach has been shown to be a simple and accurate procedure to model the geometric nonlinear displacement due to large bending displacements.[19] The formulation is based on Yang's two-dimensional formulation of a beam element used to model beams and plane frames under large deflections.[19] However, unlike Yang's work, which investigates two-dimensional structural responses due to externally applied transverse forces on beams and plane frames, the external forces applied to a three-dimensional wing structure are made up of forces and moments in the lateral, transverse, and axial directions. These forces and moments come from the aerodynamic lift, drag, and pitching moments on the wing. To model properly these forces and moments, the three-dimensional beam element is chosen with two nodes to account for all 6 DOF along the structures, leading to a 12-DOF beam element as shown in Fig. 1.

The formulation of the three-dimensional nonlinear beam equations resolves the geometric nonlinear bending displacement in the transverse and lateral directions, as well as the nonlinear twist due to the coupling of the resulting lateral, F_{drag}, and transverse, F_{lift}, forces. To demonstrate this, the deflected wing is shown in Fig. 2 with two arbitrary nodal points 1 and 2. The externally applied loads are shown at node 2, and the internal nodal moments due to the applied loads at node 2 are shown at node 1. Taking moments about node 1 due to forces at node 2 results in a transverse moment ΔM_z, a lateral moment ΔM_y, and a torsional moment ΔM_x. The transverse moment ΔM_z is due to the lift force F_{lift} multiplied by the moment arms Δx plus the side force F_{side} multiplied by the moment arms Δy. Similarly, the lateral moment ΔM_y is produced by the drag force F_{drag} and moment arms Δx.

To understand how the torsional moment ΔM_x is produced, an end view of the structure is shown in Fig. 3. The torsional moment

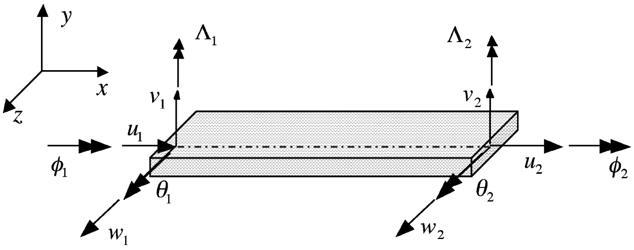

Fig. 1 Beam element, 12 DOF.

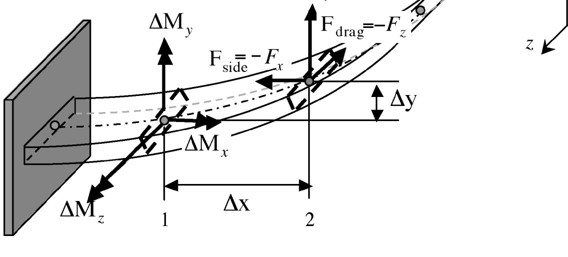

Fig. 2
Example of bending moment coupling: $\Delta M_z = F_{\mathrm{lift}} \Delta x + F_{\mathrm{side}} \Delta y$ and $\Delta M_y = F_{\mathrm{drag}} \Delta x + F_{\mathrm{side}} \Delta z$.

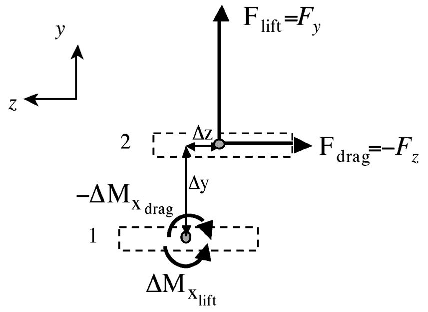

Fig. 3 End view of the beam showing bending–torsion coupling: $\Delta M_X = \Delta M_{X_{\text{lift}}} + \Delta M_{X_{\text{drag}}}$, $\Delta M_{X_{\text{drag}}} = -F_z \Delta y = F_{\text{drag}} \Delta y$, and $\Delta M_{X_{\text{lift}}} = F_y \Delta_z = F_{\text{lift}} \Delta z$.

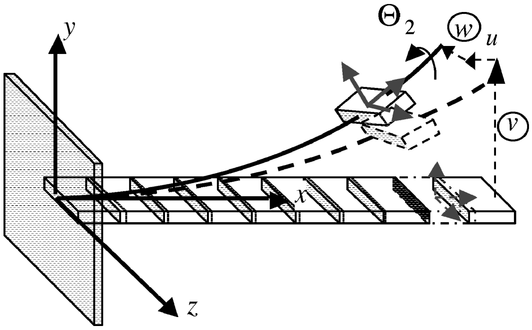

Fig. 4 Example of kinematic twist.

is produced by the lift force multiplied by the moment arm Δz and the drag force multiplied by the moment arm Δy. As can be seen in Fig. 3, the resulting torsional moment depends on the sum of the torsional moment due to the lift force, $\Delta M_{X_{\text{lift}}}$, and the torsional moment due to the drag force, $\Delta M_{X_{\text{drag}}}$. Hence, depending on whether $\Delta M_{X_{\text{lift}}}$ or $\Delta M_{X_{\text{drag}}}$ is larger, the nonlinear twist effect can either increase the twist or decrease the twist. For an aircraft wing, these moment coupling effects can be important when the wing structure is flexible in the lift direction and large enough drag loads are experienced to produce a torsional moment. This type of coupling for fixed-wing aircraft was investigated by Goetz[20] in a study of divergence including the effects of drag loads. Investigations were later conducted by Petre and Ashley in a study of drag effects on wing flutter assuming only vertical bending and twist about the elastic axis.[21] This coupling is especially true for aircraft with blunt leading-edge wings operating at high speeds, such as in transonic flow, where the drag loads increase. Also, these effects, as shown in Petre and Ashley's work, are more important for high-aspect-ratio wings.

There exists an additional twist contribution due to the kinematics of a bent line, in three dimensions, that is not captured by the three-dimensional structural model. The kinematic twist refers to the rotation of a beam section due to its transverse v and lateral w bending deflections as shown in shown in Fig. 4.[22] This additional nonlinear effect can be computed directly to second order based on the curvature equation of the three-dimensional beam as follows[22]:

$$\Theta_2 = -\int_0^L v' w'' \, \mathrm{d}L \tag{1}$$

From Eq. (1), a second-order kinematic twist correction can be obtained using the displacement functions associated with the transverse v and lateral w bending deflection expressed as follows:

$$\begin{aligned}\Theta_2 = {} & \tfrac{1}{2}(-\theta_2 + \theta_1)(\Lambda_2 + \Lambda_1) \\ & + (-\Lambda_2 + \Lambda_1)(v_2 + v_1)/L + (\theta_2 - \theta_1)(w_2 + w_1)/L\end{aligned} \tag{2}$$

(See Ref. 13 for details). Here, the preceding right-hand terms are all known rotational quantities and the twist correction is performed at the end of each FEM analysis providing an update to the most current predicted twist rotation ϕ.

Aeroelastic Equations

The static aeroelastic responses are obtained by coupling the three-dimensional nonlinear beam model to the nonlinear aerodynamic analysis using the equilibrium equation of motion.

$$[K_G(q, S)]\{q\} = \{Z\} \tag{3}$$

where $[K_G(q, S)]$ is the global nonlinear stiffness matrix. The vector $\{Z\}$ is the aerodynamic force vector obtained from the nonlinear aerodynamic analysis, and $\{q\}$ is the corresponding displacement vector. The work-equivalent load method[23] is used to transfer the computed aerodynamic loads to the beam structure through the use of the beam displacement functions. In the work-equivalent method, the work produced by the unknown nodal concentrated loads is set equal to the work produced by the applied distributed loads from the nonlinear aerodynamic analysis.[23] The nonlinear beam nodal displacements $\{q\}$ are predicted by inverting the nonlinear stiffness matrix $[K_G(q, S)]$ and then multiplying by the aerodynamic load vector $\{Z\}$. Artificial damping or relaxation is required to reduce the significant oscillations in the structural response due to the initial numerical transients of the flow solution. The current approach employs an underrelaxation method to damp these oscillations and will be discussed further in the grid movement section of this paper.

Numerical Method

The nonlinear aerodynamic model employs the upwind differencing numerical scheme, based on flux-splitting in the streamwise direction, created by Obayashi et al.[24] to solve the thin-layer Reynolds-averaged Navier–Stokes equations. The turbulence model used is the Baldwin–Lomax model.[25] Solid wall conditions are specified in the flow solver as no-slip and adiabatic. The far-field boundary flow variables are set to freestream conditions, and a symmetry plane is used at the wing root.

The three-dimensional nonlinear structural equations are solved using a second-order predictor–corrector approach. The predictor step is performed by a linearized incremental formulation of the equations, based on the approach employed by Yang,[19] where the displacements are solved incrementally by taking increments of the applied aerodynamic loading. The corrector step is obtained using a modified Newton–Raphson approach. This process is continued until the final load level is obtained and provides the nonlinear displacement path solution. Further details of the second-order predictor–corrector can be found in Ref. 13.

Geometry and Computational Meshes

Two high-aspect-ratio wings are evaluated in this study. The first wing, referred to as the BO105 wing, is an unswept rectangular high-aspect-ratio wing based on the structural properties of the BO105 helicopter blade.[26] The BO105 blade is chosen because it provides bases for an ideal set of geometric properties to test the limits of the three-dimensional nonlinear beam model. The aspect ratio of this wing is 29.0, and the elastic axis is located at 0.25% of the local chord. Neglecting the hub portion of the blade and scaling up the transverse, EI_z and lateral, EI_y stiffness values by 30%, the uniform sectional structural properties EI_z, EI_y, G_J, and EA for this wing are $3.1E{+}06$ lb/in.^{2}, $77.2E{+}06$ lb/in.^{2}, $1.69E{+}06$ lb/in.^{2}, and $1.57E{+}10$ lb, respectively. The second wing has the same properties as the unswept BO105 wing except the leading edge is sheared to achieve a leading-edge sweep of 5 deg.

The computational meshes, also known as the grids, for the fluid dynamic model is based on a C–H topology, where the C indicates the grid points wrapping chordwise around the wing airfoils and the H indicates the points in the spanwise direction. The BO105 wing surface grid is generated based on the BO105 rotor blade geometric parameters minus the hub portion of the blade.[26] The number of surface grid points used for the BO105 wing are 183 points in the C direction and 53 points in the H direction. To resolve the viscous boundary layer near the wing surface, the CFD volume mesh requires cluster points near the surface. The proper initial wall spacing distance y is achieved by maintaining an average $y^+ < 1$,

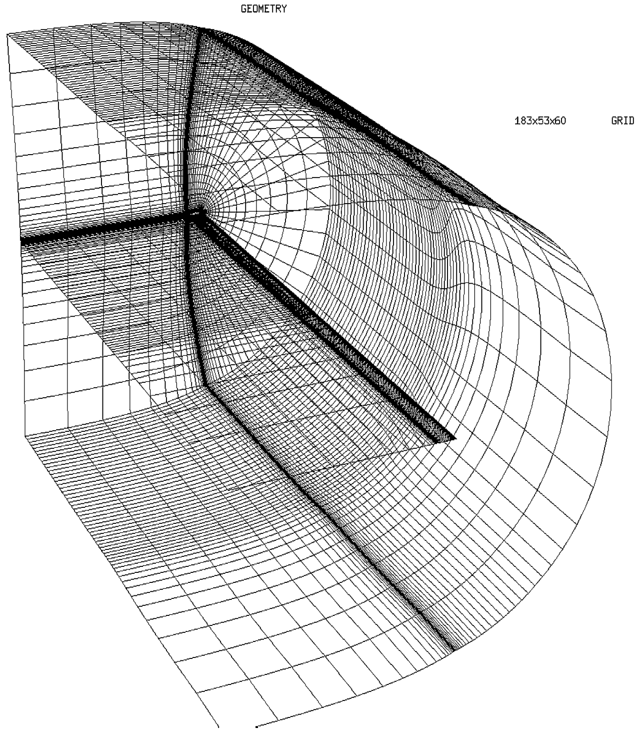

Fig. 5 Unswept high-aspect-ratio BO105 wing volume grid.

where y^+ is defined as[27]

$$y^+ = y\sqrt{\tau_w \rho}\Big/\nu_w \tag{4}$$

This leads to an average first spacing y of $1e{-}06$. The far-field boundaries are set to 10 times the wing root chord length to avoid reflections of the flow at the far-field boundaries. These requirements yield 60 points in the normal direction for the BO105 wing. The final baseline grid size for the BO105 wing is $183 \times 53 \times 60$ (Fig. 5). To verify that this was a properly sized CFD grid, a 50% finer grid of dimensions $288 \times 80 \times 90$ was used to solve the unswept nonlinear aeroelastic case. The results of this grid convergence study showed a 0.71% difference in the total drag and a 2.8% difference in total lift between the baseline and fine grid solutions. This difference verified that the baseline grid chosen was sufficient.

The structural mesh of the three-dimensional beam element is obtained by specifying the x, y, and z coordinates of each node of the elements. The selection of the number of elements is based on performing mesh convergence tests. An efficient approach to determining the number of elements for a given problem is achieved by solving the structural problem based on a set of initial applied loads distributions. The applied load distribution can come from a partially converged rigid CFD solution of the problem. This becomes useful in determining in advance the number of elements required for a converged FEM solution. Based on this approach, a minimum of 24 elements were required to capture the large nonlinear twist and bending displacements experienced by the flexible high-aspect-ratio BO105 wing.

Aeroelastic Coupling

In this study, the nonlinear aeroelastic analysis is performed using the direct coupled approach. In the direct approach, the source code of either the fluid or structural analysis is modified to perform the coupling to pass information between the fluids and structural analysis. Unlike the loosely coupled approach, the direct approach typically solves the fluid and structural analyses at every CFD time step or iteration. Hence, direct approaches are ideal for performing dynamic aeroelastic computations. Similar work done to solve the aeroelastic problem using directly coupled high-fidelity aerodynamic methods with linear structural methods can be found in Refs. 28–34. The direct approach was chosen because one of the goals of this work is to provide a framework for the future development of a nonlinear dynamic aeroelastic analysis. In the direct approach presented in this paper (Fig. 6), the distributed forces and moments are computed from the nonlinear CFD and transferred to the finite element structural nodes at the end of each CFD iteration. In the case of large transverse bending, as seen in these flexible high-aspect-ratio wings, the forces and moments need to be resolved into their $\bar{x}$, $\bar{y}$, and $\bar{z}$ components to account for the aerodynamic forces on the structure properly. Typically, in a linear analysis only the local twist of the wing is considered in determining the lift and drag of the wing. To resolve the applied forces in the three directions, a modification to the existing force and moment subroutine of the nonlinear CFD code is implemented to compute the sectional forces in the $\bar{x}$, $\bar{y}$, and $\bar{z}$ directions representing the drag, F_{drag}, side, F_{side}, and lift, F_{lift} forces, respectively. These sectional CFD forces are then interpolated onto the FEM nodal locations using a cubic spline interpolation. Then, assuming a linear load distribution between the FEM nodes, the work equivalent method[21] is used to provide the equivalent nodal force and moment vector $\{Z\}$ for the three-dimensional nonlinear beam analysis. Note that the CFD coordinate system is based on a right-handed system where the $\bar{y}$ axis is out the wing span, whereas the FEM coordinate system is a right-handed system with the x axis out the wing span. This change in coordinate system requires the proper change in sign to the forces from the CFD to be used by the FEM as shown in Fig. 7. These forces are then used by the FEM to predict the nonlinear displacements. Finally, the displacements are used to move the CFD grid, and the process repeats until the forces in the CFD analysis converge.

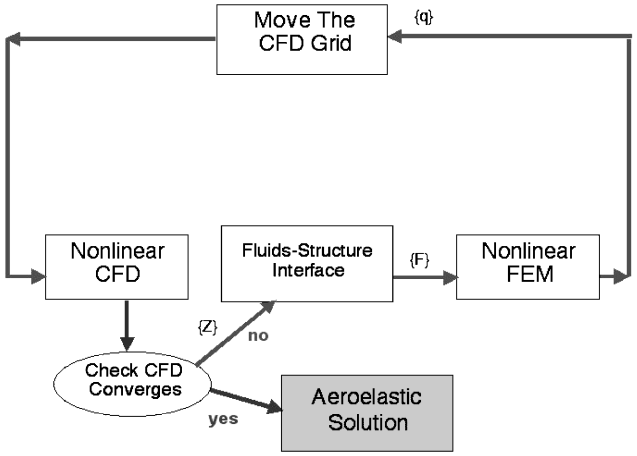

Fig. 6 Direct coupled approach.

Grid Movement

Once the FEM displacements are computed, the CFD grid is deformed consistent with these displacements. The FEM displacement values are interpolated on to the CFD grid using a cubic spline interpolation. A cubic interpolation was found necessary to provide the proper curvature on the wing surface due to the sparseness of the FEM mesh as compared to the CFD grid. Because the CFD grid uses a C–H topology, each spanwise section of the wing can be thought of as a two-dimensional plane. This allows the volume grid to be moved by translating and rotating the two-dimensional planes by the corresponding sectional transverse, axial, and twist displacements. To account for the large transverse bending rotations θ at each spanwise section, the z-coordinate values of the CFD volume grids are scaled by $1/\cos(\theta)$. This is equivalent to rotating the wing sections by the bending rotation θ and simplifies the grid movement. An example of the aeroelastic deformed grid is shown in Fig. 8.

Because of the oscillatory nature of aeroelastic solutions, damping of the structure is required. In this study the, static aeroelastic solutions are performed by starting the analysis from freestream conditions and using underrelaxation to damp the structural displacements.[34] This is achieved by computing the full nonlinear displacements based on the forces and moments predicted at

Table 1 Timing breakdown for the static aeroelastic analysis

Structures	Time for the Nonlinear Structure Analysis % Time of a CFD solver step[a]	 Total time for structures alone,[a] h	Total time for nonlinear aeroelastic,[a] h
Linear	10.23	2.93	31.6
Nonlinear	26.32	7.55	36.21

[a]Single CFD solver step = 17.7 s. [b]Timings based on 6000 iterations on a SGI R12000.

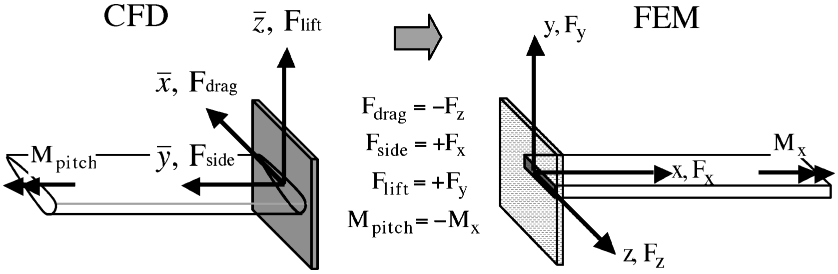

Fig. 7 CFD and FEM coordinate systems.

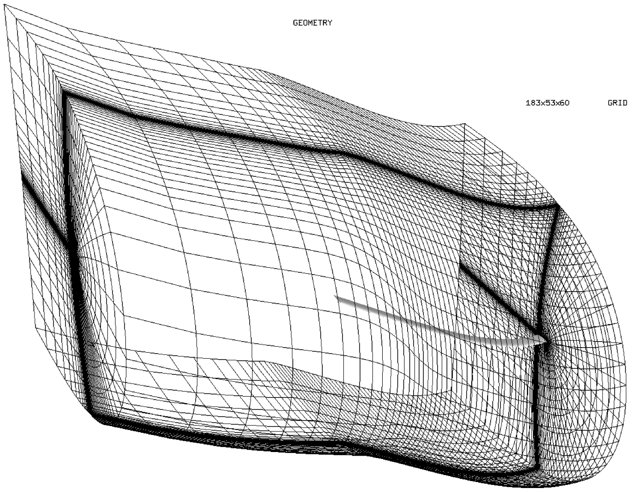

Fig. 8 Deformed CFD volume grid for the high-aspect-ratio BO105 wing.

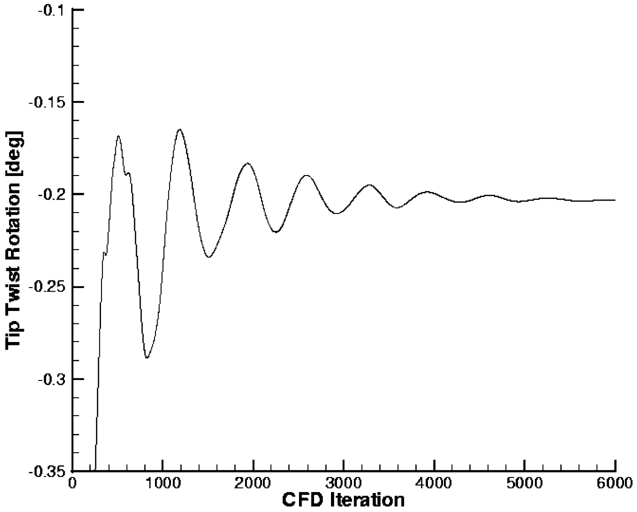

Fig. 9 Static aeroelastic convergence history for the high-aspect-ratio BO105 wing twist.

a given CFD iteration and then artificially damping these displacements by taking a percentage of the delta displacements predicted between two CFD iterations. Over many CFD iterations the delta displacements become small, and the artificial damping applied to these delta displacements becomes negligible. This method is found to be very robust for the large deflections considered. However, the aeroelastic solution is sensitive to the relaxation parameter. If the relaxation is too large, the delta displacements can be too large for the aerodynamic model to handle, and the flow solution becomes unstable. Results have shown that for deflections above 20% of the semispan, at transonic flow conditions, the number of iterations required to converge the aeroelastic solution is on the order of 6000 fluid iterations with a relaxation parameter of 0.1. A sample convergence history for tip twist of the unswept BO105 wing is shown in Fig. 9. Typical timings for the static aeroelastic analysis are shown in Table 1. The timings in Table 1 are based on a 6000 iteration aeroelastic solution of the unswept BO105 wing. The second column shows the structure time as a percentage of a single nonlinear flow solver step. For this case, the flow solver requires approximately 17.2 CPU s per iteration. The results show that the linear and nonlinear structures take 10.23 and 26.33% of a nonlinear flow solver step, respectively. Also shown in Table 1 are total times in hours for both the structures alone and the full static aeroelastic analysis.

Results and Discussion

Nonlinear aeroelastic results for the unswept BO105 wing case are computed at $M = 0.8, \alpha = 1.0$ deg, $Re = 1.2E{+}06, \gamma = 1.4$, and $q = 100$ lb/ft^2. Because of the large flexibility of this wing, a small angle of attack is used to lower the lift loads. To show the structural nonlinear effects, the aeroelastic simulation is also computed using the linear option of the nonlinear three-dimensional beam model. A comparison of transverse displacements between the nonlinear and linear three-dimensional beam solutions is shown in Fig. 10. The nonlinear structural analysis results in an effective span shortening, as seen by the tip movement in the axial direction. The linear results do not account for axial displacement, and, hence, shears the wing in the transverse direction leading to a 10% increase in the total wing span. This increase in span is a nonphysical result due to the inability of the linear model properly to account for axial displacements and maintain an inextensible wing. To remove the effect of increased span predicted by the linear solution, the span coordinate for both the linear and nonlinear results are nondimensionalized by their corresponding span lengths when shown subsequently. This allows for a direct comparison between the aerodynamic forces predicted by the linear and nonlinear structural analysis.

To demonstrate that the splining of the CFD loads and FEM displacements is sufficient, the displacements and forces for each

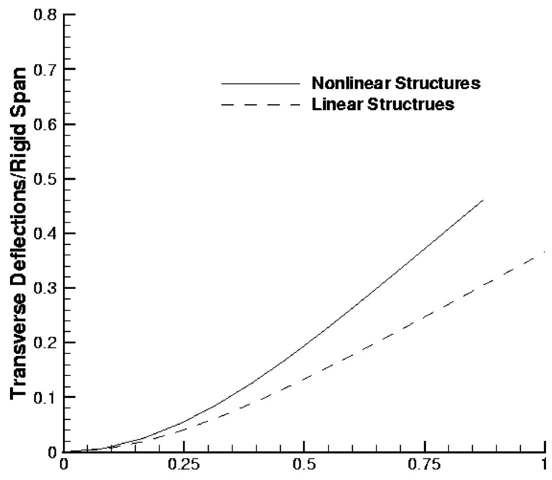

Fig. 10 Nonlinear and linear transverse bending deflection comparison for the unswept high-aspect-ratio BO105 wing.

discipline are shown for the nonlinear aeroelastic solutions of the unswept BO105 wing in Figs. 11–13. Figure 11 shows that the twist and transverse displacements are in good agreement between the CFD and FEM. Figure 12 shows the torsional moments (pitch) and transverse forces (lift) are in very good agreement. Finally, Fig. 13 shows that the axial (side) and lateral (drag) forces are also in very good agreement.

Next, static aeroelastic twist comparison between the linear and nonlinear structures approach are shown for the unswept BO105 wing (Fig. 14). The twist results show that the linear structure has a small nose-down twist rotation at the wing tip relative to the wing root, know as washout, and is attributed to the pitching moment of the airfoil sections. The nonlinear structure results show an opposite nose-up twist rotation at the wing tip relative to the wing root, known as washin, resulting in a 0.5-deg difference in the wing tip twist between the two solutions. The washin result is attributed to the nonlinear moment coupling effects of the applied aerodynamic forces, as well as the kinematic twist effects due to bending. Specifically, the large transverse bending deflections provide a moment arm for the large transonic drag force on this wing to counteract the normal pitch-down moment of the wing. To understand how this occurs, the following paragraphs will discuss in detail how the

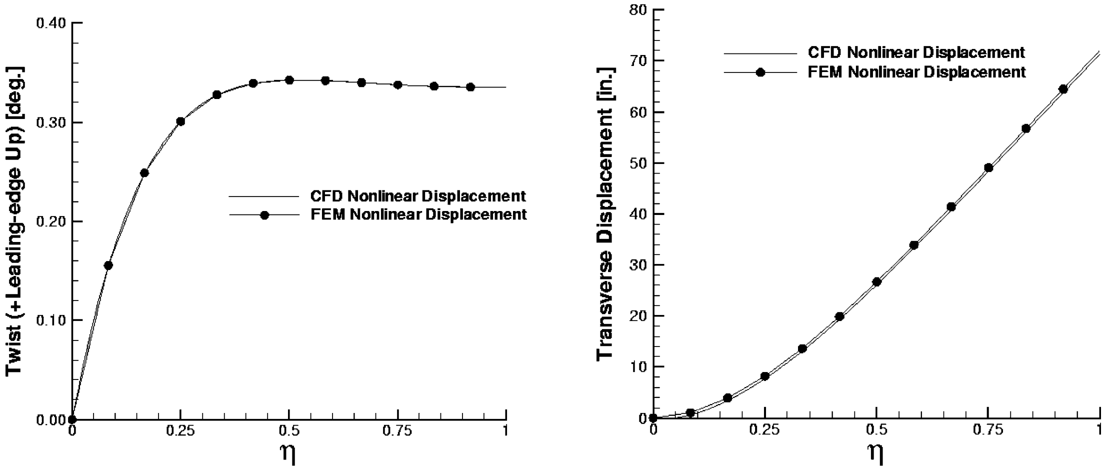

a) Twist displacement

b) Transverse displacement

Fig. 11 CFD vs FEM displacement transfer comparison of the unswept BO105 wing.

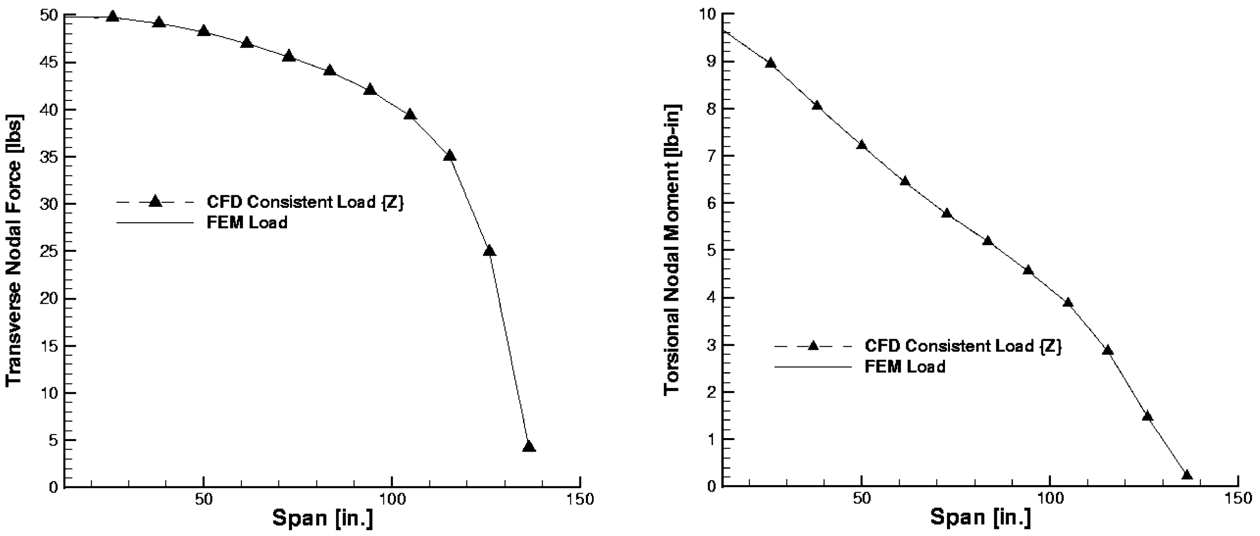

a) Transverse force (lift)

b) Torsional moment (pitch)

Fig. 12 CFD vs FEM load transfer comparison of the unswept BO105 wing: lift and pitch.

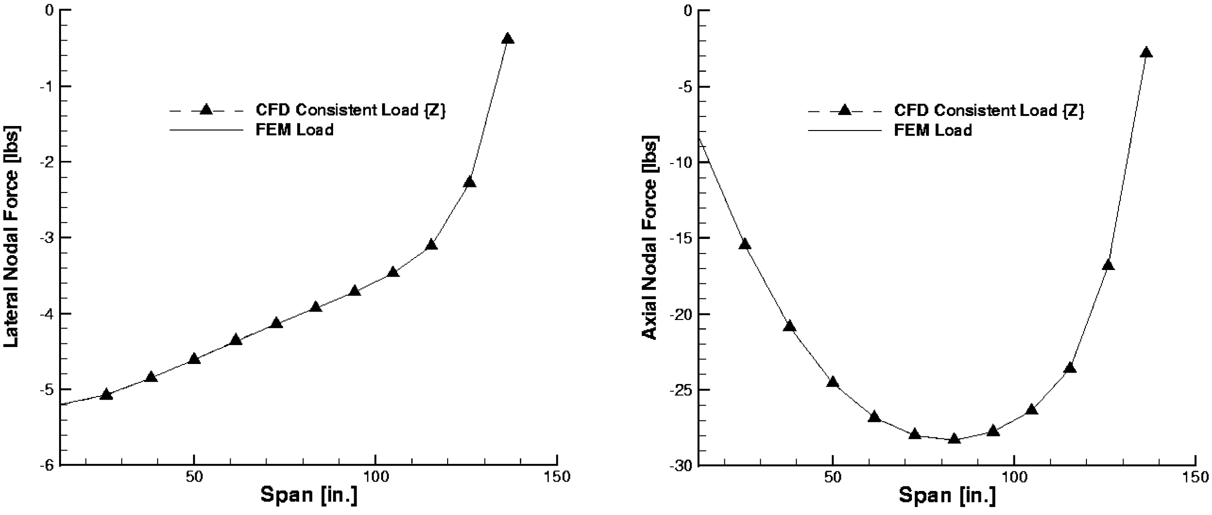

a) Lateral force (drag) **b) Axial force (side)**

Fig. 13 CFD vs FEM load transfer comparison of the unswept BO105 wing: drag and side.

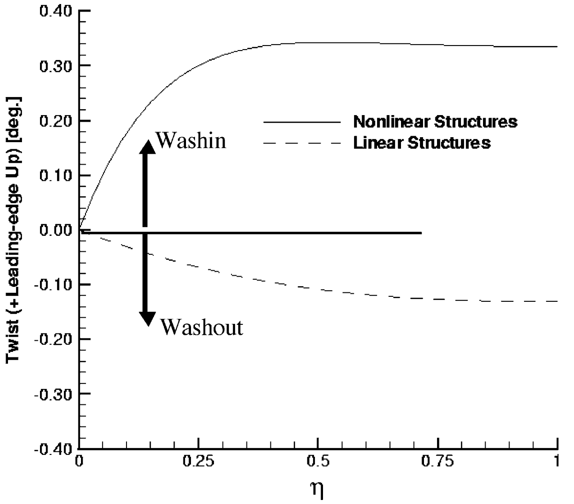

Fig. 14 Nonlinear and linear twist rotation comparison for the unswept BO105 wing.

externally applied aerodynamic forces interact with the structure to produce such a nonlinear twist result (Fig. 14).

The sectional lift coefficient results show that the linear analysis has less lift on the wing when compared to the nonlinear solution (Fig. 15a). This result agrees with the nonlinear twist indicating washin, increasing the wing lift, whereas the linear twist results lower the lift loading on the wing due to washout. Sectional drag results show larger drag for the nonlinear structural analysis compared to the linear analysis (Fig. 15b). This is again attributed to the increased local angles of attack along the wing tip for the nonlinear structure, which increases the profile and wave drag. Also note that the drag of this wing is quite large and is attributed to the strong shock on the wing as seen in the Mach number contour plot of Fig. 16.

An additional parameter describing the aerodynamic forces on the wing is the sectional side force coefficient shown in Fig. 17. The side forces represent the resulting horizontal spanwise forces due to the large transverse bending of the wing. The nonlinear side force results are approximately 40% larger in magnitude than the linear results due to the larger sectional lift forces. The shape of the side force coefficient curve resembles a parabola with a maximum at approximately midsemispan. The maximum side force corresponds to the span location where the combination of sectional lift (Fig. 15a) and spanwise slope of the wing surface (Fig. 13) are maximum. The zero side force at the root corresponds to zero surface curvature, and the zero side force at the tip corresponds to zero lift at the tip. The side force is normally not considered in linear aeroelastic methods because the deflections are small enough that the side force is negligible. However, for wings with large transverse deflection, the side force can be quite large. For this case with wing tip deflections of 40% span, the maximum sectional side force is as much as 50% of the sectional C_l.

Up to this point, the aerodynamic forces and pitching moment trends do not provide enough information to explain the nonlinear washin results at the wing tips. To investigate this nonlinear effect further, the FEM nodal forces and moments are plotted in the standard shear moment diagram form. The FEM transverse shear and moment diagrams of the wing structure are shown in Fig. 18. The nonlinear transverse shear forces and moments are larger than the linear results, which correspond to the larger sectional lift predicted by the nonlinear aeroelastic analysis. The lateral shear and moment diagrams (Fig. 19) of the wing structure show the nonlinear lateral shear forces and moments are larger in magnitude than the linear results attributed to the larger predicted sectional drag on the wing. The axial force diagram (Fig. 20) shows the nonlinear structural shear forces to be larger in magnitude than the linear corresponding to the larger side force (Fig. 17) predicted by the nonlinear structural analysis.

The results of the torsional moment diagram (Fig. 21) show that the linear structural moments are small and positive, corresponding to the small pitching moment produced by the wing aerodynamics. Note that, in the FEM coordinates (Fig. 7), a positive moment or rotation about the x axis corresponds to a washout twist rotation. However, the nonlinear structural result shows that the torsional moments M_x are much larger and negative compared to the linear results. These results are attributed to the nonlinear torsion–bending coupling on the wing structure. To understand this, refer to the deflected wing structure shown in Fig. 1. Recall, the externally applied CFD loads are shown at node 2 and the internal nodal moments due to the applied loads at node 2 are shown at node 1. Taking moments about node 1 due to the forces at node 2 results in the transverse ΔM_z, and lateral ΔM_y moments due to the lift F_{lift}, drag F_{drag}, and side F_{side} forces multiplied by the corresponding moment arms Δx, Δy, and Δz, as described earlier in the governing equation section of this paper. To understand how the torsional moment ΔM_x is produced, refer to the end view of the structure shown in Fig. 2. Recall, the torsional moment is then produced by the lift force multiplied by the moment arm Δz and the drag force multiplied by the moment arm Δy. The resulting torsional moment then depends on the sum of the torsional moment due to lift, $\Delta M_{X_{\mathrm{lift}}}$, and the torsional moment due to drag, $\Delta M_{X_{\mathrm{drag}}}$. Hence, depending on whether $\Delta M_{X_{\mathrm{lift}}}$ or $\Delta M_{X_{\mathrm{drag}}}$ is larger, the nonlinear twist effect can either increase the wing twist or decrease the wing twist. The nonlinear results for

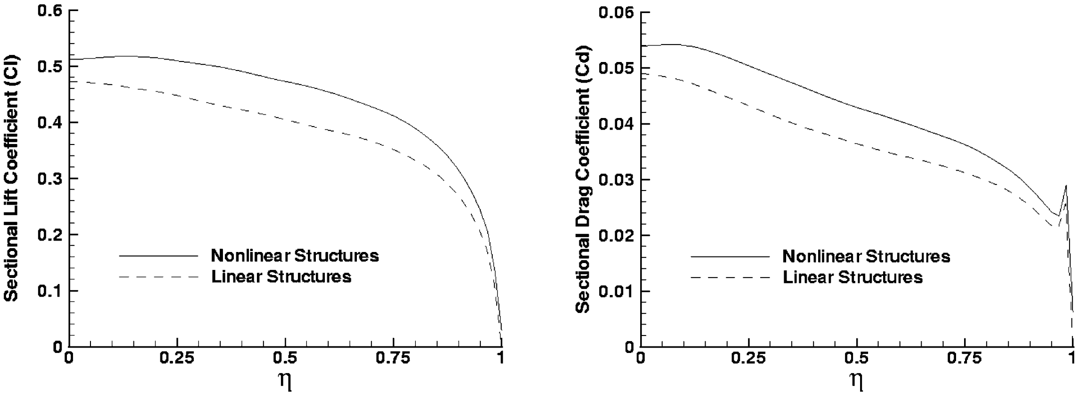

a) Sectional C_l

b) Sectional C_d

Fig. 15 Nonlinear and linear sectional C_l and C_d comparison of the unswept BO105 wing.

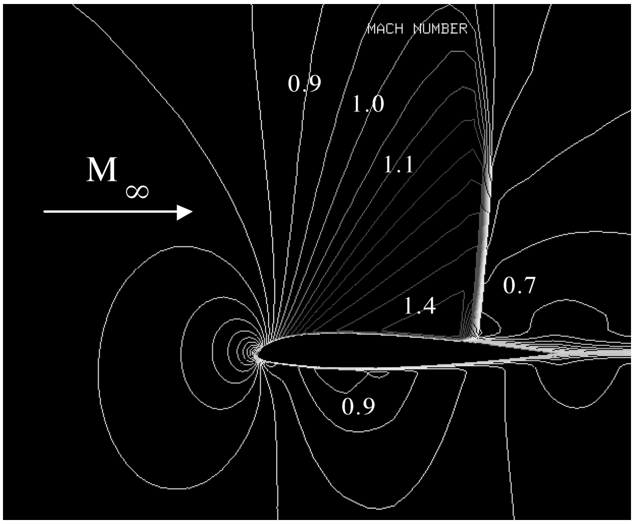

Fig. 16 Mach contours for the BO105 unswept high-aspect-ratio wing.

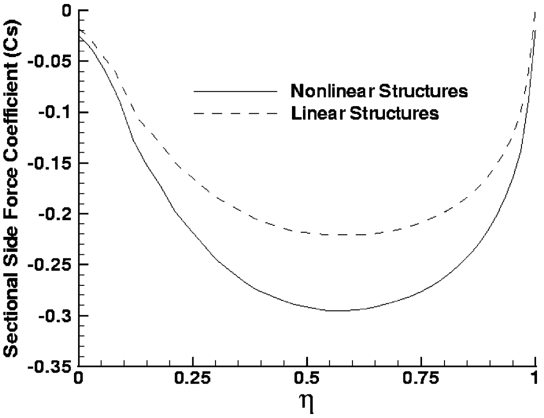

Fig. 17 Nonlinear and linear sectional side force coefficient C_s comparison for the unswept high-aspect-ratio BO105 wing.

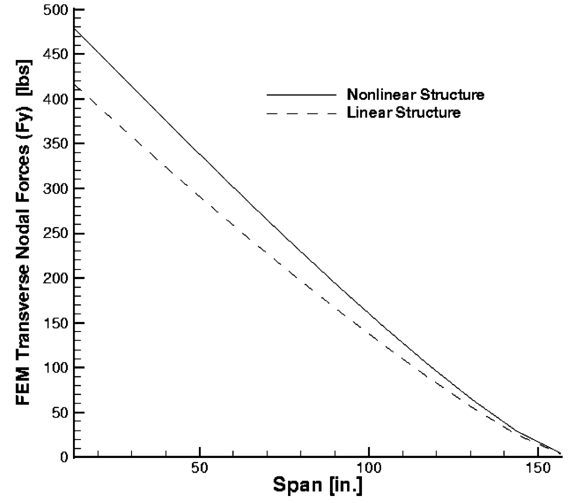

a) Transverse force F_y

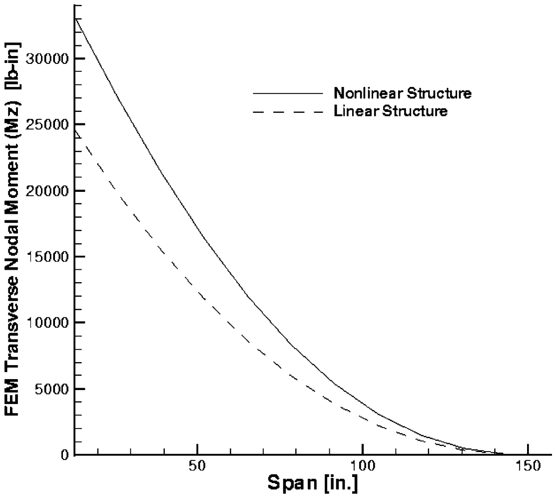

b) Transverse M_z

Fig. 18 Nonlinear and linear transverse force and moment for the unswept BO105 wing.

this wing show the torsional moments to be negative (Fig. 21), indicating that the torsional moment due to drag must be larger than the torsional moment due to lift. To verify this result, the lateral and transverse bending deflections of this wing are plotted in Fig. 22. The transverse deflections are large, and the lateral deflections are quite small. Hence, recalling the large drag forces observed on this wing in the transonic flow regime, multiplied by these large transverse bending deflections Δy, verifies that the torsional moment due to drag is larger than the torsional moment due to lift. This can explain the reverse twist response predicted earlier (Fig. 14) by the nonlinear aeroelastic analysis. These results also show how the nonlinear aerodynamics in the transonic flow can influence the nonlinear structural response of these wings. Finally, the kinematic effects of twist due to bending deflections are shown by replotting the nonlinear twist with and without the kinematic effects (Fig. 23). The results show that the kinematic bending effects tend to increase twist on the unswept wing as described by Eqs. (1) and (2), which creates additional washin on the wing.

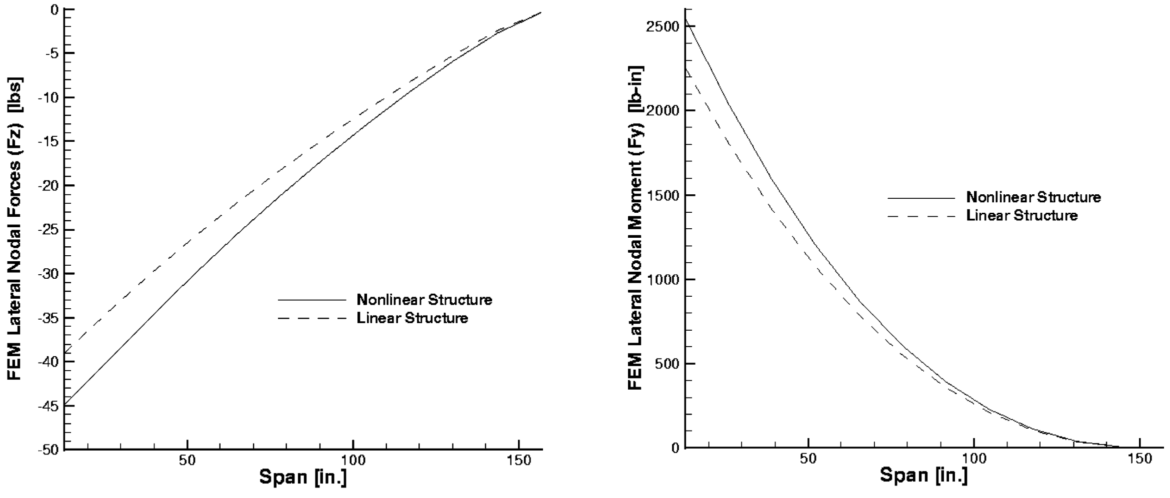

a) Lateral force F_z

b) Lateral moment M_y

Fig. 19 Nonlinear and linear lateral force and moment for the unswept BO105 wing.

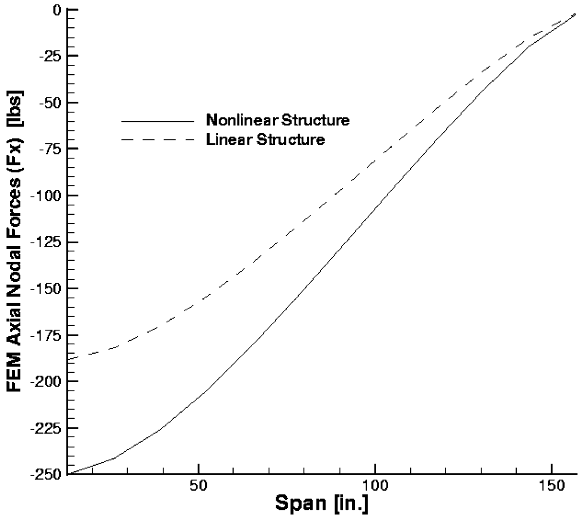

Fig. 20 Nonlinear and linear axial shear force for the unswept BO105 wing.

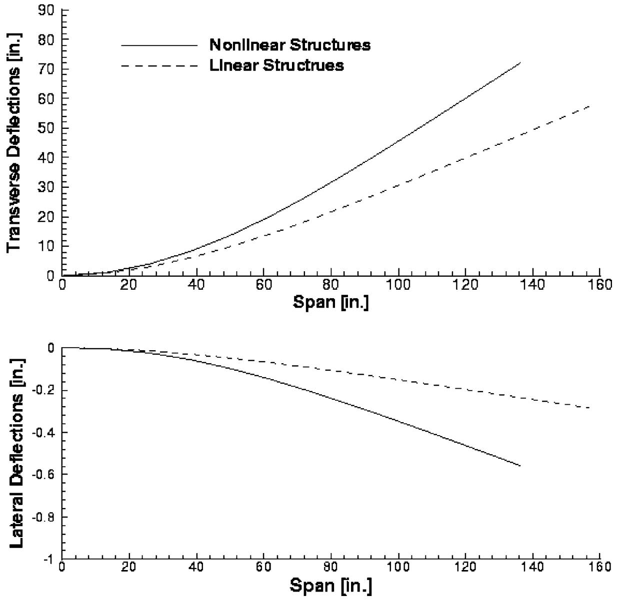

Fig. 22 Nonlinear transverse and lateral deflections for the unswept BO105 wing.

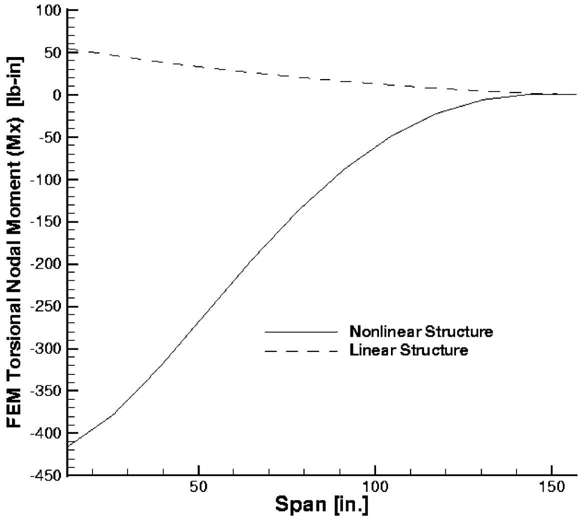

Fig. 21 Nonlinear and linear torsional moment M_x for the unswept BO105 wing.

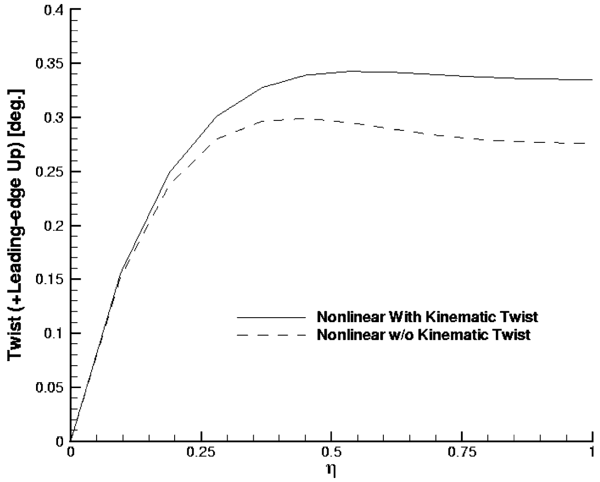

Fig. 23 Effects of kinematic twist on the unswept high-aspect-ratio BO105 wing.

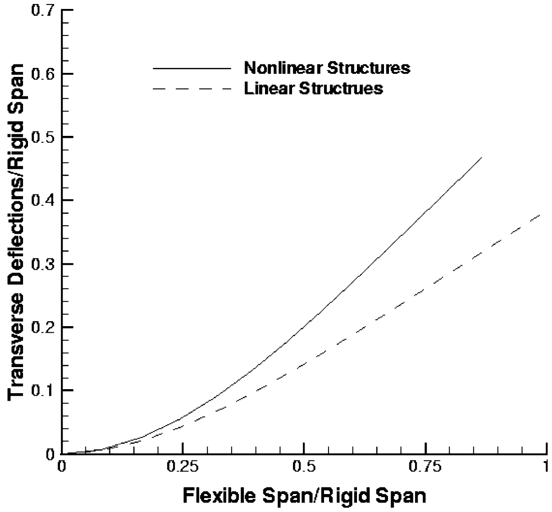

Fig. 24 Nonlinear and linear transverse bending deflection for the swept BO105 wing.

The nonlinear effects of the swept high-aspect-ratio BO105 wing are studied next. The aeroelastic results for this case are computed at $M = 0.8$, $\alpha = 4.0$ deg, $Re = 1.2E{+}06$, $\gamma = 1.4$, and $q = 100$ lb/ft^2. Note that an angle of attack of 4 deg is used to approximately match the wing tip deflections with those of the unswept BO105 wing. Increasing the root angle of attack is done to counter the basic swept-back wing effects of twist due to bending, which for upward bending reduces the local angle of attack on the wing toward the tip, referred to as washout.[11]

The aeroelastic results of the transverse deflection comparison between the nonlinear and linear three-dimensional beam solutions show similar trends to the unswept wing (Fig. 24). The sectional wing twist (Fig. 25) shows both the nonlinear and linear results to have a large amount of washout, which is attributed to the swept wing twist effects due to bending deflections. However, the nonlinear structure results show the wing to have approximately 0.5 deg less washout. The nonlinear result is attributed to the nonlinear moment coupling effects as well as the kinematic twist effects due to bending. To understand how the externally applied aerodynamic forces interact with the structure to produce the nonlinear twist results (Fig. 25), the sectional lift, drag, and side force coefficients are plotted. Sectional lift coefficient results show that the linear solution

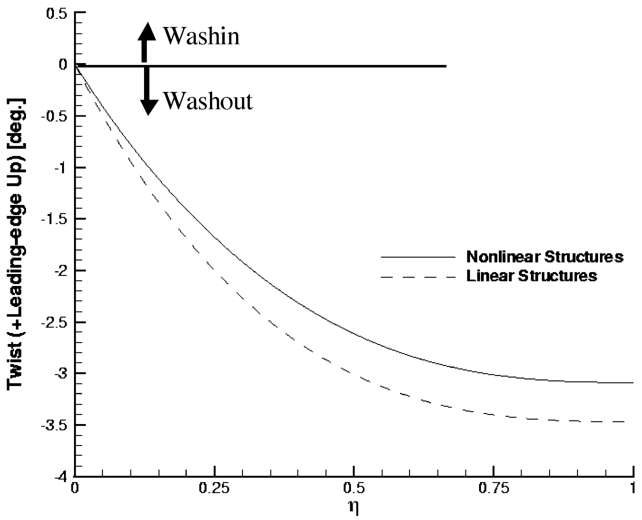

Fig. 25 Nonlinear and linear twist rotation comparison for the swept BO105 wing.

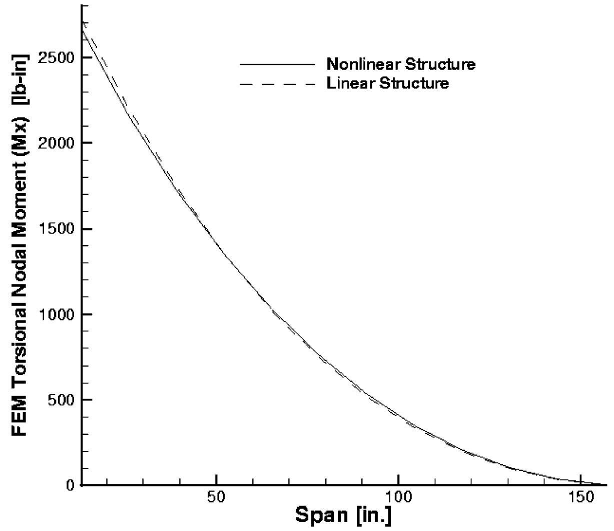

Fig. 27 Nonlinear and linear torsional moment M_x for the swept BO105 wing.

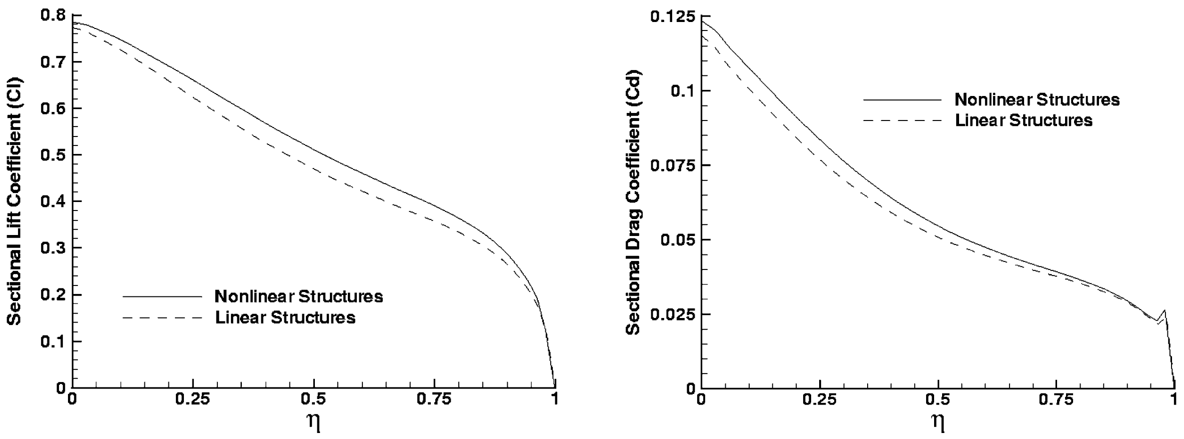

a) Sectional C_l **b) Sectional C_d**

Fig. 26 Nonlinear and linear sectional C_l and C_d comparison for the swept BO105 wing.

predicts less lift on the wing as compared to the nonlinear solution (Fig. 26a). This corresponds to the prediction of larger washout for the linear structure lowering the lift loading on the wing. Sectional drag results show larger drag for the nonlinear structural analysis compared to the linear analysis (Fig. 26b). This is attributed to the larger local angles of attack at the wing tip for the nonlinear structure, which increases the profile and wave drag. As in the unswept wing case, the drag of this wing is quite large and is attributed to the strong shocks present at these transonic flow conditions. The side force C_s results are found to have the same trend as the unswept wing, where the magnitude of the nonlinear structural results are approximately 70% larger than the linear results.

To further investigate the nonlinear twist result, the torsional moment diagram of the wing structure is shown in Fig. 27. The linear and nonlinear torsional moments results are very similar (Fig. 27). This appears to shows that the net effect of the nonlinear torsion due to lift $\Delta M_{X_{\text{lift}}}$ and drag $\Delta M_{X_{\text{drag}}}$ cancel out, unlike the unswept wing.

Finally, the nonlinear twist results with and without the kinematic twist effects are shown in Fig. 28. The kinematic effects reduce the washout produced by the sweptwing bending deflections by as much as 0.82 deg. This is attributed to the large positive transverse and lateral bending deflections shown in Fig. 29. This can be explained by referring to the kinematic twist equation (2) and by noting that a positive transverse and lateral bending will produce a net negative twist, which in the FEM global coordinates is a leading-edge up twist rotation. This leading-edge up twist rotation reduces the amount of washout on the swept wing and makes the wing more prone to tip stall. The result shows how that the combination of the kinematics, the nonlinear torsion–bending coupling, the aerodynamic loads, and the elastic twist due to bending of the sweptwing interact to produce the nonlinear aeroelastic twist effects.

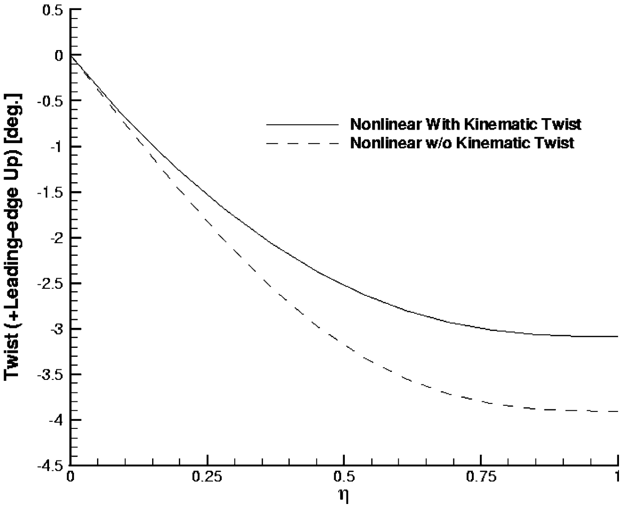

Fig. 28 Effects of kinematic twist on the swept high-aspect-ratio BO105 wing.

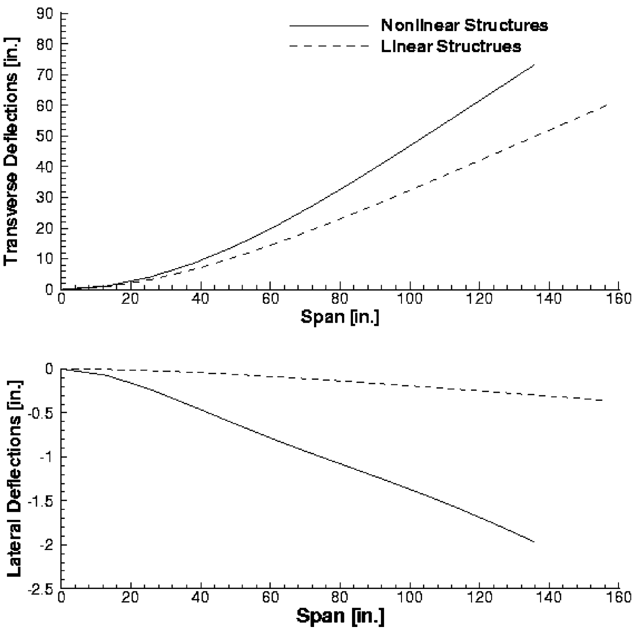

Fig. 29 Nonlinear transverse and lateral deflections for the swept BO105 wing.

Conclusions

The development of a nonlinear aeroelastic analysis that directly couples a three-dimensional nonlinear beam model to a high-fidelity nonlinear CFD model is presented.

Static aeroelastic results using the developed nonlinear aeroelastic analysis show that for an unswept wing a reversal in wing twist occurs due to nonlinear torsion–bending coupling effects. Specifically, the torsional moments due to drag become large enough to cause the wing twist rotations to washin the wing tips, whereas the linear results show a washout twist rotation. The nonlinear twist results are attributed to the large bending deflections coupled with the large drag experienced by these flexible high-aspect-ratio wings at the transonic flow conditions, which the linear analysis does not account for.

Static nonlinear aeroelastic analysis results of a swept high-aspect-ratio flexible wing show that the nonlinear torsion–bending effect, due to the kinematics of the bent wing structure, becomes the dominant effect and tends to reduce the amount of washout of the wing as compared to linear results. Overall, the swept wing twists in the linear and nonlinear structural analyses indicate washout due to the strong linear bending–torsion coupling inherent in swept wings. However, the nonlinear effects tend to reduce the amount of washout on the wing, making it more prone to tip stall.

It has been demonstrated that the nonlinear static aeroelastic characteristics of flexible high-aspect-ratio wings in transonic flow are different than the linear aeroelastic results. These differences are attributed to the coupling of the drag force, at transonic speeds, with the large transverse bending deflections, as well as the kinematic effects of the bent wing structure. Both effects create a nonlinear torsional response and make the wing more susceptible to static aeroelastic problems such as wing divergence.

References

[1] *New World Vistas: Air and Space Power for the 21st Century*, U.S. Air Force Scientific Advisory Board Report, Summary Vol., 1995.

[2] Johnson, F. P., "Sensor Craft: Tomorrow's Eyes and Ears of the Warfighter," AIAA Paper 2001-4370, Aug. 2001.

[3] Van Shoor, M. C., and Von Flotow, A. H., "Aeroelastic Characteristics of a Highly Flexible Aircraft," *Journal of Aircraft*, Vol. 27, No. 10, 1990, pp. 901–908.

[4] Pendaries, C., "From the HALE Gnopter to the Ornithopter—or How to Take Advantage of Aircraft Flexibility," *21st Congress of the International Council of the Aeronautical Sciences*, Paper A98-31715, Sept. 1998.

[5] Patil, M. J., Hodges, D. H., and Cesnik, C. E. S., "Nonlinear Aeroelasticity and Flight Dynamics of High-Altitude Long-Endurance Aircraft," *Journal of Aircraft*, Vol. 38, No. 1, 2001, pp. 88–94; also AIAA Paper 99-1470, April 1999.

[6] Patil, M. J., and Hodges, D. H., "On the Importance of Aerodynamic and Structural Geometric Nonlinearities in Aeroelastic Behavior of High-Aspect-Ratio Wings," AIAA Paper 2000-1448, April 2000.

[7] Tang, D., and Dowell, E. H., "Experimental and Theoretical Study of Aeroelastic Response of High-Aspect-Ratio Wings," *AIAA Journal*, Vol. 39, No. 8, 2001, pp. 1430–1441.

[8] Greer, D., Hamory, P., Krake, K., and Drela, M., "Design and Predictions for High-Altitude (Low Reynolds Number) Aerodynamic Flight Experiment," *Journal of Aircraft*, Vol. 37, No. 4, 2000, pp. 684–689.

[9] Huttsell, L., Schuster, D., Volk, J., Giesing, J., and Love, M., "Evaluation of Computational Aeroelasticity Codes for Loads and Flutter," AIAA Paper 2001-0569, Jan. 2001.

[10] Jones, R. T., *Wing Theory*, Princeton Univ. Press, Princeton, NJ, 1990, pp. 90–104.

[11] Bisplinghoff, R. L., Ashley, H., and Halfman, R. L., Aeroelasticity, Dover, New York, 1983, pp. 1–14.

[12] Guruswamy, G. P., "User's Guide for ENSAERO—A Multidisciplinary Program for Fluid/Structure/Control Interaction Studies of Aircraft (Release 1)," NASA TM 108853, Oct. 1994.

[13] Garcia, J. A., "A Numerical Investigation of Nonlinear Aeroelastic Effects on Flexible High Aspect Ratio Wings," Ph.D. Dissertation, Aeronautical and Astronautical Engineering Dept., Stanford Univ., Stanford, CA, June 2002.

[14] Hodges, D. H., and Dowell, E. H., "Nonlinear Equations of Motion for the Elastic Bending and Torsion of Twisted Nonuniform Rotor Blades," NASA TN D-7818, Dec. 1974.

[15] Minguet, P., and Dugundji, J., "Experiments and Analysis for Composite Blades Under Large Deflections, Part 1: Static Behavior," *AIAA Journal*, Vol. 28, No. 9, 1990, pp. 1573–1579.

[16] Gallagher, R. H., *Finite Element Analysis—Fundamentals*, Prentice–Hall, Englewood Cliffs, NJ, 1975.

[17] Bathe, K.-J., and Wilson, E. L., *Numerical Methods in Finite Element Analysis*, Prentice–Hall, Englewood Cliffs, NJ, 1976, pp. 151–162.

[18] Rao, S. S., *The Finite Element Method in Engineering*, Pergamon, Maxwell House, Fairview Park, New York, 1980, pp. 291–298.

[19] Yang, T. Y., "Matrix Displacement Solution to Elastica Problems of Beams and Frames," *International Journal of Solids and Structures*, Vol. 9, 1973, pp. 829–842.

[20] Goetz, R. C., "Divergence of Some All-Movable Control Surfaces Including Drag Loading," NASA TN D-4793, Oct. 1968.

[21] Petre, A., and Ashley, H., "Drag Effects on Wing Flutter," *Journal of Aircraft*, Vol. 13, No. 10, 1976, pp. 755–763.

[22] Johnson, W., "Rotorcraft Dynamics Models for a Comprehensive Analysis," American Helicopter Society 54th Annual Forum, May 1998.

[23] Yang T. Y., *Finite Element Structural Analysis*, Prentice–Hall, Englewood Cliffs, NJ, 1986, pp. 143–147.

[24] Obayashi, S., Guruswamy, G. P., and Goorjian, P. M., "Streamwise Upwind Algorithm for Computing Unsteady Transonic Flows Past Oscillating Wings," *AIAA Journal*, Vol. 29, No. 10, 1991, pp. 1668–1677.

[25] Baldwin, B. S., and Lomax, H. L., "Thin Layer Approximation and Algebraic Model for Separated Turbulent Flows," AIAA Paper 78-257, Jan. 1978.

[26] Staley, J. A., "Validation of Rotorcraft Flight Simulation Program Through Correlation with Flight Data for Soft-Inplane Hingeless Rotor," U.S. Army Air Mobility Research and Development Lab., Rept. USAAMRDL-TR-75-50, Jan. 1975.

[27] Anderson, D. A., Tannehill, J. C., and Pletcher, R. H., *Computational Fluid Mechanics and Heat Transfer*, McGraw Hill, New York, 1984, pp. 222–225.

[28] Guruswamy, G. P., and Yang, T. Y., "Aeroelastic Time-Response Analysis of Thin Airfoils by Transonic Code LTRAN2," *Computers and Fluids*, Vol. 9, No. 4, 1980, pp. 409–425.

[29] Hooker, J. R., Burner, A. W., and Valla, R., "Static Aeroelastic Analysis of Transonic Wind Tunnel Models Using Finite Element Methods," AIAA Paper 97-2243, June 1997.

[30] Guruswamy, G. P., and Byun, C., "Direct Coupling of Euler Flow Equations with Plate Finite Element Structures," *AIAA Journal*, Vol. 33, No. 2, 1995, pp. 375–377.

[31] Nathman, J. K., and Barton, J. M., "Aeroelastic Calculations with an Euler Code," AIAA Paper 97-2271, June 1997.

[32] Robinson, B. A., Batina, J. T., and Yang, T. Y., "Aeroelastic Analysis of Wings Using the Euler Equations with a Deforming Mesh," *Journal of Aircraft*, Vol. 28, No. 11, 1991, pp. 778–788.

[33] Reuther, J. J., Alonso, J. J., Martins, J. R. R. A., and Smith, S. C., "A Coupled Aero-Structural Optimization Method for Complete Aircraft Configurations," AIAA Paper 99-0187, Jan. 1999.

[34] Eldred, L. B., Byun, C., and Guruswamy, G. P., "Integration of High Fidelity Structural Analysis into Parallel Multidisciplinary Aircraft Analysis," AIAA Paper 98-2075, April 1998.